ACS Photonics

pubs.acs.org/journal/apchd5

Article

Understanding and Controlling Mode Hybridization in Multicavity Optical Resonators Using Quantum Theory and the Surface Forces Apparatus

Bruno Zappone,* Vincenzo Caligiuri,* Aniket Patra, Roman Krahne, and Antonio De Luca

Cite This: https://doi.org/10.1021/acsphotonics.1c01055

Read Online

ACCESS | Metrics & More | Article Recommendations | Supporting Information

ABSTRACT: Optical fields in metal-dielectric multilayers display typical features of quantum systems, such as energy level quantization and avoided crossing, underpinned by an isomorphism between the Helmholtz and Schrödinger wave equations. This article builds on the fundamental concepts and methods of quantum theory to facilitate the understanding and design of multicavity resonators. It also introduces the surface forces apparatus (SFA) as a powerful tool for rapid, continuous, and extensive characterization of mode dispersion and hybridization. Instead of fabricating many different resonators, two equal metal-dielectric-metal microcavities were created on glass lenses and displaced relative to each other in a transparent silicone oil using the SFA. The fluid thickness was controlled in real time with nanometer accuracy from more than 50 μm to less than 20 nm, reaching mechanical contact between the outer cavities in a few minutes. The fluid gap acted as a third microcavity providing optical coupling and producing a complex pattern of resonance splitting as a function of the variable thickness. An optical wave in this symmetric three-cavity resonator emulated a quantum particle with nonzero mass in a potential comprising three square wells. Interference between the wells produced a 3-fold splitting of degenerate energy levels due to hybridization. The experimental results could be explained using the standard methods and formalism of quantum mechanics, including symmetry operators and the variational method. Notably, the interaction between square wells produced bonding, antibonding, and nonbonding states that are analogous to hybridized molecular orbitals and are relevant to the design of "epsilon-near-zero" devices with vanishing dielectric permittivity.

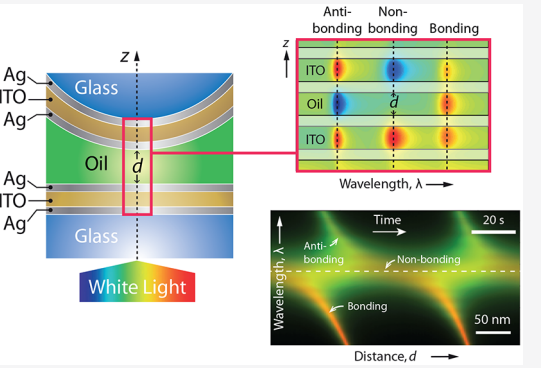

KEYWORDS: *optical cavity, surface forces apparatus, quantum analogy, metal-dielectric multilayer, epsilon-near-zero modes*

Analogies between optics and quantum mechanics date back to the foundation of quantum theory and continue to stimulate a fruitful exchange of ideas between these fields.[1,2] For instance, non-Hermitian systems with parity-time symmetry[3,4] and spin−orbit coupling in complex electronic structures[5] are actively investigated with the help of photonic emulators providing "synthetic" Hamiltonians. Quantum theory also underpins the study of bound states in the continuum (BIC),[6−8] which can be found in photonic structures such as photonic crystals[9−12] and double-bend waveguides.[12] It has long been known that the Helmholtz equation for optical waves in transparent dielectric materials is isomorphic to the steady-state Schrödinger equation for quantum wave functions.[1,13] An electromagnetic field with time dependence $e^{-i\omega t}$ in a uniform isotropic material satisfies the Helmholtz wave equation $\nabla^2\psi + \varepsilon(\omega/c)^2\psi = 0$, where ψ is a component of the electric or magnetic field, ε is the dielectric permittivity, and c is the speed of light. Although the permittivity generally is a complex number, it can be approximated as a positive real number $\varepsilon = n_D^2 > 0$ in a nonabsorbing transparent dielectric at optical frequencies, where n_D is the refractive index. On the other hand, the imaginary part of ε is much larger than the real part in metals such as Ag and Mg, so that the permittivity can be approximated as a negative real number $\varepsilon = \kappa_M^2 < 0$, where κ_M is the extinction coefficient.[14] Because the quantity $\varepsilon(\omega/c)^2$ is always close to a real number in a metal-dielectric structure, the Helmholtz equation is formally equivalent to the Schrödinger equation $\nabla^2\psi + (2m/\hbar^2)(\mathcal{E} - V)\psi = 0$, describing a hypothetical quantum particle with mass m and energy $\mathcal{E}$ in a potential V, where $\varepsilon(\omega/c)^2$ plays the role of $(2m/\hbar^2)(\mathcal{E} - V)$.

A transparent dielectric corresponds to a region of space where $\mathcal{E}$ is larger than V, namely $\mathcal{E} = V + (\varepsilon/2m)(\hbar\omega/c)^2$ with

Received: July 13, 2021

$\varepsilon > 0$, whereas a nonabsorbing metal with $\varepsilon < 0$ corresponds to $\mathcal{E} < V$ (Figure 1). A piece-wise uniform synthetic potential V

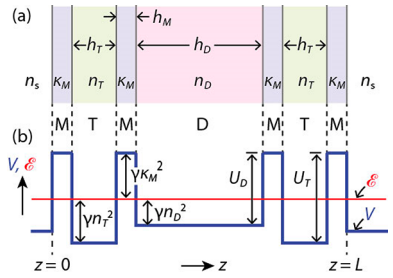

Figure 1. (a) Planar multilayer comprising metal (M) and transparent dielectric (T) layers with fixed thickness h_M and h_T, respectively, and a transparent dielectric film (D) with variable thickness h_D. The outer MTM cavities and central MDM cavity form a symmetric three-cavity resonator (MTMDMTM). n_T, n_D, and n_s are the refractive index of the T and D layers, and of the surrounding dielectric medium, respectively, whereas κ_M is the metal extinction coefficient. (b) Synthetic quantum potential V comprising three square wells with depths U_T or U_D, corresponding to the T and D layers. $\mathcal{E}$ is the energy of the quantum particle and $\gamma = (\hbar\omega/c)^2/2m$.

can be obtained simply by joining materials with different real permittivities. The potential undergoes a step-like variation at the interface between a transparent dielectric and a non-adsorbing metal, increasing by the quantity $U = (\hbar\omega/c)^2(n_D^2 + \kappa_M^2)/2m$ from the dielectric into the metal (Figure 1). Through the Helmholtz–Schrödinger isomorphism, quantum mechanics provides a powerful theoretical toolbox to understand the optics of metal-dielectric structures. Vice versa, typical quantum features such as energy level quantization and hybridization can be engineered, controlled, and studied more conveniently in metal-dielectric structures than in genuine quantum systems.

From both the experimental and conceptual points of view, the simplest metal-dielectric optical device is the planar cavity obtained by sandwiching a layer of solid dielectric material (T) between two partially reflecting metal layers (M). Such MTM cavity, also known as Fabry–Perot etalon,[15,16] can be obtained by sequential vapor deposition or sputtering of the M and T materials on glass.[17] Multiple-beam interference between light waves bouncing on the metal mirrors modulates the cavity's optical transmittance, producing a discrete sequence of sharp resonance peaks at wavelengths λ_p, where p is the chromatic order of the resonance mode (Figure 2, red curves).

The transmittance can be precisely calculated using standard methods such as transfer matrix multiplication (see Supporting Information, SI, for details on the method).[15,18] Cavity resonators are widely used in interferometry,[15] lasers,[19] spectroscopy and molecular sensing,[20] color filters, super-absorbers,[21] thin-film studies[22] and surface force measurements.[23] Moreover, a MTM cavity can be described as a single homogeneous layer with an effective dielectric response such that the real part of the permittivity crosses zero at resonance, while the imaginary part becomes very small.[14] Such "epsilon-near-zero" (ENZ) permittivity is associated with many intriguing phenomena, including nonlinearity enhancement,[24] negative refraction,[25,26] ultrafast optical switching,[27] adiabatic frequency shifting,[28] intraband optical conductivity,[29] phase singularity,[30] and appearance of Casimir forces.[31] Compared to natural ENZ materials such as Ag and indium–tin-oxide (ITO), waveguides[32] and hyperbolic metamaterials,[33] metal-

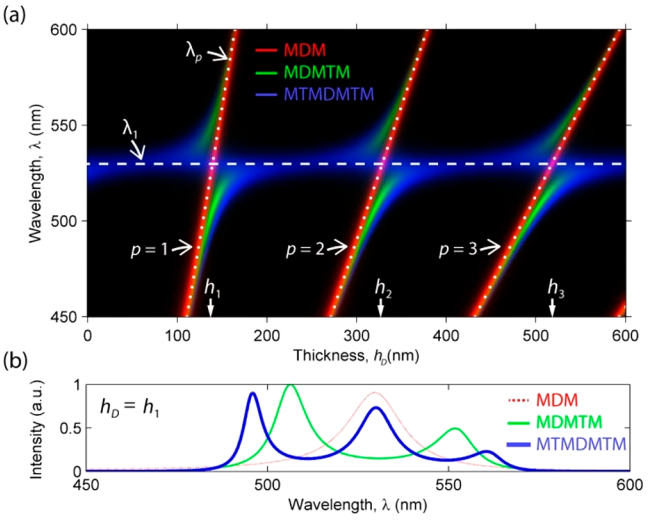

Figure 2. (a) Transmittance under normal incidence calculated with the transfer matrix method for a single cavity (MDM, red), asymmetric two-cavity resonator (MDMTM, green), and symmetric three-cavity resonator (MTMDMTM, blue). M, T, and D indicate respectively a metal (Ag), rigid transparent material (ITO), and deformable transparent dielectric (silicone oil). The transmittance is shown as a function of the thickness h_D of the D layer and wavelength λ. Resonances correspond to local intensity maxima. The M and T layers had thickness h_M = 40 nm and h_T = 85 nm, respectively. The T and D layers had refractive indices of n_T = 1.9 and n_D = 1.4, respectively. White dots indicate the resonant wavelengths of the MDM cavity calculated as $\lambda_p \approx 2nh_D^*/p$ where p is the resonance order and $h_D^* = h_D + 50$ nm is an effective thickness. λ_1 is the first resonant wavelength of a single MTM cavity. The wavelengths λ_p of a single MDM cavity cross λ_1 at thicknesses $h_D = h_1, h_2, ..., h_p$. (b) Transmitted spectra for the thickness $h_D = h_1$ showing a 2-fold wavelength splitting (green curve) or 3-fold splitting (thick blue curve) for the MDMTM and MTMDMTM resonator, respectively, compared to the single resonance (dotted red curve) of the MDM cavity.

dielectric cavity resonators provide a simple and flexible design of ENZ modes with low losses in the visible spectrum, which can be used to engineer strong light-matter coupling.[34]

Multicavity planar resonators can be obtained by stacking two or more metal-dielectric cavities with shared metal layers. In an asymmetric two-cavity resonator (MTMDM) with a deformable dielectric (D) layer, the coupling between resonance modes of the MTM cavity (e.g., Figure 2a, dashed horizontal line with wavelength λ_1) and MDM cavity (Figure 2a, dotted lines with wavelengths λ_p) leads to avoided crossings (Figure 2a, green curves at thicknesses $h_D = h_1, h_2, ...$) and splitting of resonance wavelengths (Figure 2b, green curve). These effects are due to the hybridization of single-cavity modes analogous to the creation of delocalized molecular orbitals from single-atom orbitals.[34] The analogy can be extended to periodic cavity resonators, showing ENZ photonic bands similar to electron bands in solid-state crystals.[35] Yet, a theoretical and mathematical framework is needed to calculate the optical coupling strength and explain how the complex dispersion of a multicavity resonator originates from the simple responses of individual cavities.

This article introduces the surface forces apparatus (SFA) as a powerful tool to study the modal dispersion of multicavity resonators. Cavity thickness was varied rapidly, continuously, extensively, and with nanometer accuracy. This allowed

https://doi.org/10.1021/acsphotonics.1c01055
ACS Photonics XXXX, XXX, XXX−XXX

measuring the dispersion as a function of cavity thickness (as in Figure 2a), avoiding the costly and time-consuming experimental task of fabricating multiple resonators with different thicknesses. We validated this approach for symmetric three-cavity resonators (MTMDMTM) with a deformable dielectric layer (D), exhibiting a pattern of 3-fold wavelength splitting (Figure 2, blue color). On the basis of the Helmholtz–Schrödinger isomorphism with a quantum potential comprising three interfering square wells, our study shows that the 3-fold splitting reflects the formation of a "nonbonding" hybrid mode in addition to the "bonding" and "antibonding" modes of a two-cavity resonator. Interestingly, the nonbonding mode is insensitive to variations of optical thickness in the central D layer.

We anticipate that the SFA can be used to study virtually any planar optical multilayer as a function of the thickness of one or more layers, for example, to characterize the coupling of epsilon-near-zero modes with excitons embedded in a fluid or create planar optical metamaterials with tunable optical response. Our findings also have implications in the design and interpretation of SFA experiments on the electrochemistry of surfaces and the electrification of nanoscale fluid films, typically involving multicavity metal-dielectric resonators.[36−39]

RESULTS

Transmittance of a Single Cavity. Rigid MTM microcavities were fabricated by sputtering deposition of Ag and ITO on glass with target thickness h_M = 40 nm and h_T = 80 nm, respectively. The cavities were produced both on planar glass slides and on the cylindrical lenses used in SFA experiments, which have a diameter of 1 cm and curvature radius R = 2 cm (Figure 3a). The transmittance of planar cavities was measured by ellipsometry and showed a peak at wavelength λ_1 = 520 nm, with full width at half-maximum of about 40 nm.

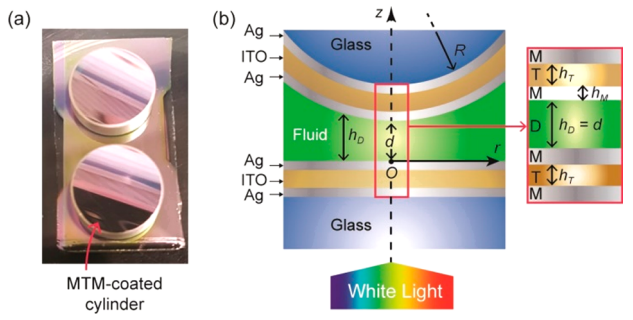

Figure 3. (a) MTM microcavities fabricated on the SFA cylindrical lenses having 1 cm diameter and radius of curvature R = 2 cm. The M and T layers were made of Ag and ITO, respectively. (b) Schematic of the SFA setup with two MTM-coated cylinders facing each other in silicone oil (D) at distance d apart. The cylinder axes are crossed at 90°, ensuring a single surface contact point (r = 0, dashed vertical line) around which the surface separation distance h_D approximates a sphere-plane geometry (eq 1). The inset shows the planar MTMDMTM resonator obtained at the contact point.

The transmittance of a single cavity (MDM) with variable thickness h_D was calculated as a function of the wavelength λ using the transfer matrix method (Figure 2, red curves).[15] For ideal perfectly reflecting metal layers with zero electric resistivity, the resonant modes of a MDM cavity are confined within the D layer. Multiple-beam interference produces a set of "quantized" wavelengths $\lambda_p = 2n_Dh_D/p$, corresponding to resonant modes with different order p = 1, 2, 3, ..., where n_D is the refractive index of the D layer.[15] In real metals with finite conductivity, the field extends into the M layer over a distance $\delta \approx \lambda/2\pi\kappa$ known as skin depth, where κ is the metal extinction coefficient, producing a red-shift of the resonance wavelengths. For Ag, $\kappa \approx 3$ is almost constant and $\delta \approx 27$ nm varies less than 10% across the optical spectrum (450−600 nm wavelengths).

Figure 2 shows that the resonance wavelengths of a single cavity vary as a function of the thickness h_D according to an approximately linear relation: $\lambda_p = 2n_Dh_D^*/p$, where $h_D^* > h_D$ is an effective thickness including the skin depth.[22] In particular, the 520 nm peak of planar rigid MTM cavities corresponded to the first resonant mode with $\lambda_1 \approx 2n_Th_T^*$, where n_T = 1.8 and h_T^* = 144 nm are the ITO refractive index and effective thickness, respectively. Note that h_T^* is close to $h_T + 2\delta \approx 134$ nm, where h_T is the target ITO thickness.

Dispersion of a Three-Cavity Resonator. The SFA was originally developed to measure surface interactions in fluid films and soft materials with nanoscale thickness.[40,41] The material is confined between two cylindrical solid surfaces with a radius of curvature R of a few cm, which are mounted in a sealed enclosure at a distance d apart with their cylinder axes crossed at 90°, ensuring a single contact position (Figure 3b). The surface separation distance is

$$h_D \approx d + r^2/2R \quad (1)$$

approximating a sphere-plane geometry at small lateral distances $r \ll R$ from the contact position (r = 0). The top surface is fixed to a rigid mount, whereas the bottom surface is attached to the free end of a two-spring cantilever. The distance d can be varied with nanoscale accuracy by displacing the fixed cantilever end with precision linear actuators. In this work, two MTM-coated cylindrical lenses (Figure 3a) were approached at a distance d in silicone oil (Figure 3b). The fluid gap (D) between the two rigid cavities acted as a third deformable microcavity (MDM), coupling the outer rigid cavities in a symmetric three-cavity resonator (MTMDMTM) with variable thickness of the D layer (Figure 1, Figure 2, blue color, and Figure 3b, inset). The optical transmittance was measured under normal incidence at the surface contact point (r = 0, Figure 3b) while varying the surface distance d from more than 50 μm to less than 20 nm, reaching direct mechanical contact between the MTM cavities, in a single sweep taking less than 10 min. This amounted to varying the thickness d of the fluid film in the central cavity (MDM) while keeping the outer cavities (MTM) unchanged.

Transfer matrix calculations show that the avoided crossing between resonances of the central fluid cavity (MDM) and outer rigid cavities (MTM) leads to a 3-fold splitting of the resonant wavelength (Figure 2, blue curves). The calculations also show that the central wavelength of the triplet is almost constant as a function of the fluid film thickness h_D and close to the first-mode wavelength λ_1 of the outer cavities. Moreover, the resonance of the three-cavity resonator (Figure 2, blue curves) overlaps with that of a single MDM cavity (Figure 2, red curves and white dots) outside the avoided crossing region, i.e., when h_D is far from h_p or, equivalently, when λ_p is far from λ_1.

These features were reproduced in SFA experiments (Figure 4a). The intensity I transmitted at the contact point (r = 0, Figure 3b) was measured as a function of the wavelength λ and time while displacing the fixed end of the cantilever at a

https://doi.org/10.1021/acsphotonics.1c01055
ACS Photonics XXXX, XXX, XXX−XXX

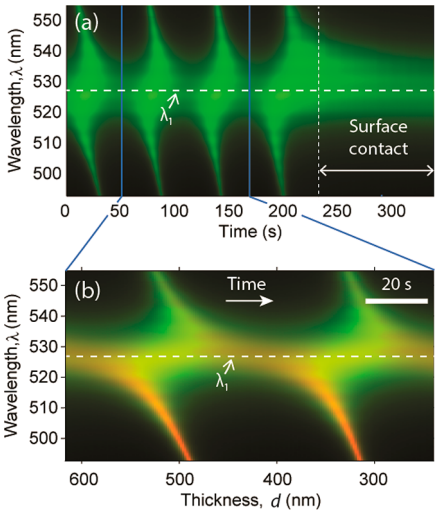

Figure 4. (a) Experimental SFA spectrogram showing the intensity transmitted by a symmetric three-cavity resonator (MTMDMTM) at the contact position (r = 0 in Figure 3b) as a function of time and wavelength λ during surface approach with cantilever speed u = 3.3 nm/s. In the surface contact region, a mechanical force slowed the surface motion and time evolution of the transmitted spectrum. λ_1 is the first-order wavelength of the outer MTM cavities. (b) Overlay of the experimental spectrogram (green) and calculated transmittance (red) showing the noncontact region where the surface distance d varied uniformly with speed u. Overlapping intensities appear orange. In the transfer matrix calculation, the M and T layers had thickness h_M = 37 nm and h_T = 84 nm, respectively, and the D layer had refractive index n_D = 1.41.

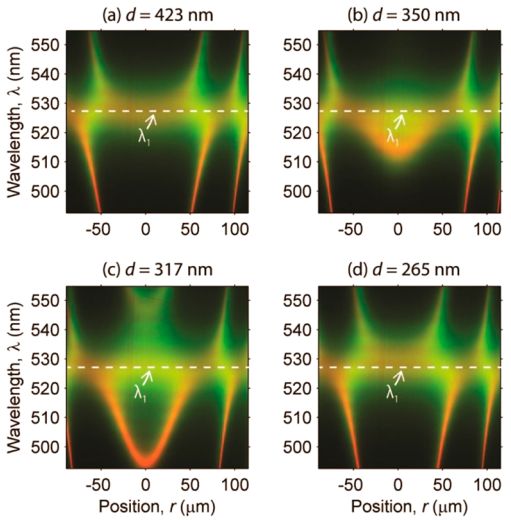

Figure 5. Experimental (green) and simulated (red) spectrographs showing the intensity transmitted by the MTMDMTM resonator as a function of the wavelength λ and lateral position r for different surface separation distances d. The surfaces were continuously approached going from (a) to (d). λ_1 is the first-order wavelength of the outer MTM cavities. The transfer matrix calculation parameters are the same as in Figure 4b.

constant speed u = 3.3 nm/s. At large distances d, surface interactions were negligible.

The cantilever was not deflected and the bottom surface was displaced at the same speed as the cantilever, i.e., $\partial d/\partial t = u$ (Figure 4a, left side). Therefore, the evolution of the transmission spectrum as a function of time corresponded to a linear variation of the fluid thickness d with time. When the surfaces reached contact, a repulsive mechanical force deflected the cantilever. The bottom surface moved at speed $\partial d/\partial t < u$, and therefore, the time evolution of the spectrum slowed (Figure 4a, right side). The experimental $I(d, \lambda)$ spectrograms showed local transmission peaks arranged in S-shaped fringes that were connected by a thickness-independent horizontal band, centered at wavelength λ_1 = 520 nm (Figure 4a). These findings could be reproduced using transfer matrix calculations (Figure 4b), displaying the same features as in Figure 2. Namely, the S-shaped fringes appeared at fluid thicknesses close to h_p, where a 3-fold resonance splitting was expected, and the horizontal band corresponded to the central wavelength of the triplet, close to the resonant wavelength λ_1 of the MTM cavities.

The SFA setup includes an imaging spectrograph that resolves the intensity I as a function of the wavelength λ and lateral distance r from the contact position (Figure 5).[40] For a fixed distance d, the resonant wavelengths varied as a function of r in a way that reflected the dependence of r on h_D. Namely, h_D increased parabolically with r (eq 1) and the resonant wavelength increased almost linear with h_D far from λ_1 (Figure 2). In this region, therefore, the resonance fringes $\lambda(r)$ had a parabolic shape. A single $I(r, \lambda)$ spectrograms could be obtained in less than a second and covered a range of thickness h_D of about 300 nm, from d to $d + r_{max}^2/2R$, where $r_{max} \approx 100$ μm is half the field of view of the spectrograph.

DISCUSSION

Quantum Theory in a Multiwell Potential. Consider a multicavity resonator with total thickness L and layer normal z, so that z = 0 and $z = L$ correspond to the resonator's entrance and exit, respectively (Figure 1b). Under the condition of normal incidence used in SFA experiments, the Helmholtz–Schrödinger isomorphism applies to any transverse component ψ of the electric or magnetic field in any layer of the resonator (under oblique incidence, the isomorphism is valid only for transverse-electric plane waves, as shown in SI).

The resonator's transmittance is proportional to the square modulus $|\psi|^2$ for $z > L$. This is equivalent to the probability $|\psi(z > L)|^2$ of finding the quantum particle past the potential V created by the metal (M) and dielectric (T, D) layers (Figure 1). Electromagnetic field penetration in the M layers with skin depth $\delta = c/(2\kappa\omega)$ is analogous to quantum tunneling in a potential barrier, with a tunneling distance equal $\delta = [2m(U - \mathcal{E})/\hbar^2]^{-1/2}$. Adopting the quantum formalism, we denote with $|\psi\rangle$ an electromagnetic mode with wave function $\psi(z)$ and introduce the complex scalar product $\langle\psi_1|\psi_2\rangle = \int\psi_2^*\psi_1\, dz$. The Helmholtz–Schrödinger isomorphism maps resonant modes into quantum eigenstates $|\psi\rangle$ of a synthetic Hamiltonian with wave function representation:

$$\mathcal{H} = -(\hbar^2/2m)\partial^2/\partial z^2 + V \quad (2)$$

Indeed, the resonator's transmittance is different from zero at a frequency ω only if a nonzero solution ψ exists for the Helmholtz equation at that frequency. The same wave function is a solution of the Schrödinger equation $\mathcal{H}|\psi\rangle = \mathcal{E}|\psi\rangle$, where $\mathcal{E}$ is the energy. Note that $\mathcal{E}$, V, and $\mathcal{E} - V$ depend on the frequency ω, and the energy zero is arbitrary.

Because $V > \mathcal{E}$ in the metal, whereas $V < \mathcal{E}$ in the dielectric materials, the synthetic potential V in eq 2 comprises a series of square wells corresponding to the T and D layers (Figure 1b).

https://doi.org/10.1021/acsphotonics.1c01055
ACS Photonics XXXX, XXX, XXX–XXX

If the outer metal layers of the resonator are considered infinitely thick and the energy zero is in the metal, the synthetic potential is $V = \Sigma_\alpha V_\alpha$, where V_α is the square well potential corresponding to a single cavity. Namely, $V_\alpha = U = -(\hbar^2 k^2/2m)(n_D^2 + \kappa_M^2)$ in the well and $V_\alpha = 0$ elsewhere.[14]

Solutions to the wave equation for a single square well with potential V_α can be found in various textbooks on quantum mechanics.[42−44] Because in our case $\mathcal{E} \leq 0$ (Figure 1b), the energy eigenstates $|\alpha_p\rangle$ of a single cavity are bound states, i.e., the quantum particle is localized mainly in the well (a method for creating free particle states such that $\mathcal{E} > \max(V)$ is outlined in SI). The eigenstate wave function ψ_α is real and has a defined wavevector modulus $nk_p = p\pi/h_\alpha^*$, where p is the "quantum number" corresponding to the chromatic order, and h_α^* is an effective width. The mode of order p has a nondegenerate energy $\mathcal{E}_{\alpha,p} = (\hbar^2/2m)(nk_p)^2$. The potential V_α is invariant under the spatial inversion $z \to -z$ about the center of the well. Therefore, the single-cavity Hamiltonian, $\mathcal{H}_\alpha = -(\hbar^2/2m)\partial^2/\partial z^2 + V_\alpha$, commutes with the inversion operator and energy eigenstates $|\alpha_p\rangle$ have a defined parity. Namely, eigenstates with odd or even order p are even or odd, respectively.[42−44]

Solutions of the Schrödinger equation for a double square well potential can be found in quantum physics textbooks.[45] Multiple square wells appear in the study of stacked semiconductor quantum wells, chains of quantum dots, and Bose−Einstein condensates.[46] Examples of multiple coupled resonators abound in mechanics, electronics, optics, and photonics and can be analyzed using general methods such as coupled-mode theory and coupled-oscillator models.[47−50] In this work, we present a method of analysis based on a three-well potential that reproduces the experimental findings (Figures 4 and 5), establishes a clear connection with well-known concepts and methods of quantum mechanics, and allows direct calculation of the coupling coefficients and wavelength splitting.

A symmetric MTMDMTM resonator is analogous to a symmetric three-well synthetic potential (Figure 1b). In the absence of interference between wells, the energy eigenstates $|\alpha_p\rangle = |l_p\rangle$ and $|\alpha_p\rangle = |r_p\rangle$ of the left and right well, respectively, have equal order p and equal energy $\mathcal{E}_{o,p}$, whereas the eigenstates $|c_q\rangle$ of the central well with order q have *a priori* different energies. For three noninterfering wells, the energy $\mathcal{E}$ is nondegenerate when it matches a level $\mathcal{E}_{c,q}$ of the central well but none of the levels $\mathcal{E}_{o,p}$ of the outer wells. A 2-fold degeneracy is found when $\mathcal{E}$ matches a level of the outer wells without matching any level $\mathcal{E}_{c,q}$ of the central well. A 3-fold degeneracy is found when $\mathcal{E} = \mathcal{E}_{o,p} = \mathcal{E}_{c,q}$. When the refractive index is the same in all cavities, the 3-fold degeneracy occurs when the ratio h_D^*/h_T^* between the widths of central and outer cavities is a rational number, so that $q/h_D^* = p/h_T^*$ for a suitable choice of integers p and q (Figure 1).

Variational Method Analysis. In our experiments, the distance h_M between wells, that is the thickness of the metal layers, was comparable but larger than the tunneling length (skin depth) δ (Figure 1). Therefore, the wave function overlap between neighboring wells was small. To quantify the wavelength splitting and coupling strength, we use the Rayleigh−Ritz variational method, a classical tool to study the hybridization of atomic orbitals in molecular quantum theory.[36,41] Namely, hybridized states are written as linear combination $|\psi\rangle = \Sigma_\alpha a_\alpha |\alpha_p\rangle$ of the energy eigenstates $|\alpha_p\rangle$ of isolated noninterfering wells. The coefficients a_α are obtained by applying the variational condition $\partial\mathcal{E}/\partial a_\alpha = 0$, where $\mathcal{E} = \langle\psi|\mathcal{H}\psi\rangle/\langle\psi|\psi\rangle$ is the average energy of $|\psi\rangle$ and $\mathcal{H}$ is the total Hamiltonian of the interfering wells (eq 2).

Because SFA spectrographs only captured the wavelength $\lambda_1 = 520$ nm of the first-order states $|l_1\rangle$ and $|r_1\rangle$ for the outer wells (Figures 4 and 5), we only consider the hybridization of these states with the states $|c_q\rangle$ of the central well. Quantum perturbation theory shows that the hybridization is strongest for the $|c_q\rangle$ state with energy $\mathcal{E}_{c,q}$ closest to the first-order energy $\mathcal{E}_{1l} = \mathcal{E}_{1r}$ of the left and right wells.[42,51] Therefore, trial functions for the variational method can be written as

$$|\psi\rangle = a_l|l_1\rangle + a_r|r_1\rangle + a_c|c_q\rangle \tag{3}$$

These functions should be eigenstates of the symmetry operator P that inverts the z-axis about the midpoint of the central well ($z = L/2$ in Figure 1b). The operator P exchanges $|l_1\rangle$ and $|r_1\rangle$, that is $P|l_1\rangle = |r_1\rangle$ and $P|r_1\rangle = |l_1\rangle$, so that the combinations $|g_1\rangle = (|l_1\rangle + |r_1\rangle)/\sqrt{2}$ and $|u_1\rangle = (|l_1\rangle - |r_1\rangle)/\sqrt{2}$ are even and odd, respectively (Figure 6a, left side). In particular, the first-order even state $|c_1\rangle$ can be combined with $|g_1\rangle$ to create the even states:

$$|\psi\rangle = a_g|g_1\rangle + a_c|c_1\rangle \tag{4}$$

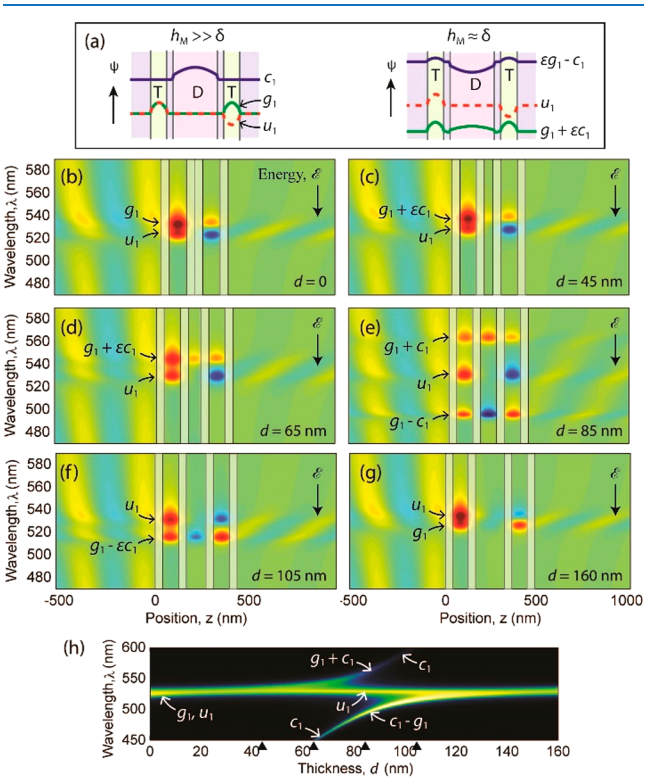

Figure 6. (a) First-order states of the central cavity ($|c_1\rangle$) and of the outer cavities ($|g_1\rangle$ and $|u_1\rangle$), shown to the left, produce the hybridized states shown to the right for a metal thickness $h_M \approx \delta$. ϵ is a positive hybridization coefficient. (b−g) Real part of the electric field calculated as a function of the position z along the layer normal and wavelength λ for various thicknesses d of the central fluid layer (D). The resonator was illuminated under normal incidence from the left side ($z < 0$). Shaded areas indicate the metal (M) layers. (h) Calculated transmittance. The transfer matrix calculation parameters are the same as in Figure 4b.

https://doi.org/10.1021/acsphotonics.1c01055
ACS Photonics XXXX, XXX, XXX−XXX

with a suitable choice of the coefficients a_g and a_c (Figure 6a, right side). On the other hand, $|c_1\rangle$ cannot create a state with defined parity by mixing with $|u_1\rangle$, which therefore is the only odd hybrid state.

Bonding, Antibonding, and Nonbonding Modes. To connect SFA experiments (Figures 4 and 5) and quantum theory, suppose to increase the width h_D of the central well/cavity. For $h_D = 0$, the coefficient $a_c = 0$ should be used in eq 3 and therefore the trial functions are $|\psi\rangle = |g_1\rangle$ and $|\psi\rangle = |u_1\rangle$. Since the left and right cavities are in direct contact (MTMMTM), they can couple to each other through the double metal layer at the center. This layer, however, acts as an effective double-width barrier to tunneling and hinders wave function overlap between the cavities. As shown in the SI, a negligible overlap leads to a negligible difference between the energies $\mathcal{E}_{1g}$ and $\mathcal{E}_{1u}$ of the states $|g_1\rangle$ and $|u_1\rangle$, respectively. This also entails that $\mathcal{E}_{1g}$ and $\mathcal{E}_{1u}$ are practically equal to the first-order energy $\mathcal{E}_{1l} = \mathcal{E}_{1r}$ of noninterfering outer wells. The absence of energy splitting explains why transfer matrix calculations (Figure 2, blue curves) and SFA spectrograms (Figure 4) do not show any significant splitting of the first-order wavelength λ_1 for a vanishing thickness h_D of the central cavity. The splitting and symmetry of the $|g_1\rangle$ and $|u_1\rangle$ states are highlighted by transfer matrix calculations in Figure 6b, showing the real part of the electric field. On the other hand, it has been shown that a thick central metal layer increases the quality factor of a two-cavity resonator, which behaves as a superabsorber.[34,52] Moreover, the resonator shows ENZ permittivity at resonance.[34]

As the thickness h_D of the central well increases, the level $\mathcal{E}_{1c}$ of the central-well state $|c_1\rangle$ approaches from above the level $\mathcal{E}_{1g} \approx \mathcal{E}_{1u}$ of the outer-well states $|g_1\rangle$ and $|u_1\rangle$. Because $|u_1\rangle$ does not mix with $|c_1\rangle$ and has negligible intensity within the inner cavity (Figure 6b–g), $|u_1\rangle$ is practically independent of the thickness h_D and refractive index n_D of the central cavity. This type of state is called "non-bonding" in molecular orbital theory[53] and corresponds to the horizontal band with wavelength λ_1 observed in the calculated (Figure 2) and experimental SFA spectrograms (Figures 4 and 5) for all thicknesses h_D. On the other hand, the states $|g_1\rangle$ and $|c_1\rangle$ become increasingly hybridized as h_D increases and $\mathcal{E}_{1c}$ approaches $\mathcal{E}_{1g} \approx \mathcal{E}_{1u}$. Applying the variational conditions to the even trial function of eq 4 we obtain

$$\Sigma_{\mu,\nu} a_\mu (H_{\mu\nu} - \mathcal{E}\langle\mu|\nu\rangle) = 0 \tag{5}$$

where the indices μ and ν indicate $|g_1\rangle$ and $|c_1\rangle$, and $H_{\mu\nu} = \langle\mu|\mathcal{H}|\nu\rangle$ are the matrix elements of the total Hamiltonian $\mathcal{H}$ of the three interfering wells. Eq 5 admits two solutions with different energies $\mathcal{E}$ and coefficient ratios a_c/a_g. When the energy difference $\mathcal{E}_{1c} - \mathcal{E}_{1g}$ is large, the ratio a_c/a_g is either very large or very small, meaning that the hybridization is weak.[42,51] The former case corresponds to a state close to $|c_1\rangle$, whereas the latter corresponds to a state close to $|g_1\rangle$ (indicated respectively as and $\varepsilon|g_1\rangle - |c_1\rangle$ and $|g_1\rangle + \varepsilon|c_1\rangle$ in Figure 6a, right side). As h_D and $\mathcal{E}_{1c} - \mathcal{E}_{1g}$ decrease, the hybridization becomes stronger and the energy level of the $|c_1\rangle$-like state pushes the level of the $|g_1\rangle$-like state toward lower energies (compare Figures 2 and 4 with Figure 6c–f). This sort of repulsion demonstrates the von Neumann–Wigner level avoidance rule, according to which the levels of two hybridized states with the same symmetry cannot cross as a function of the single parameter h_D.[51]

As h_D equals the thickness h_T of the left and right wells (Figure 1), and $\mathcal{E}_{1c}$ reaches $\mathcal{E}_{1g}$, the hybridization becomes strongest. As shown in the SI for three interfering wells having the same depth U and width h_D, eq 5 leads to the two even hybrid states $|\pm\rangle = (|c_1\rangle \pm |g_1\rangle)/\sqrt{2}$ with different energies $\mathcal{E}_\pm$ $\chi \approx \mathcal{E}_1 \pm \chi U$. Here, χ is the overlap integral between $|c_1\rangle$ and $|g_1\rangle$ restricted to either the central well or the outer wells. Since $\chi U < 0$, the $|+\rangle$ state has energy $\mathcal{E}_+ < \mathcal{E}_1$ and "bonding" character, whereas the $|-\rangle$ state has energy $\mathcal{E}_- > \mathcal{E}_1$ and "antibonding" character. We stress that the variational method allows calculating *a priori* the off-diagonal matrix elements $H_{\mu\nu}$ representing the coupling strength and, therefore, the splitting $\mathcal{E}_+ - \mathcal{E}_-$ (as shown in SI), in contrast with other methods where phenomenological coupling parameters must be determined *a posteriori*.[50] Figure 6e shows that the coupling produces a triplet state with the bonding and antibonding wavelength symmetrically spaced from the wavelength λ_1 of the nonbonding state, as expected from simulations (Figure 2) and observed experimentally (Figure 4b). Note that coupling and interference between the wells completely removes the triple degeneracy of the energy level $\mathcal{E}_{1c} = \mathcal{E}_{1u} = \mathcal{E}_{1g}$ expected for $h_D{}^* = h_T{}^*$.

When the level $\mathcal{E}_{1u} = \mathcal{E}_{1g}$ is approached from above by the next level $\mathcal{E}_{2c}$ of the central cavity, the odd state $|c_2\rangle$ is hybridized with $|u_1\rangle$ and pushes the perturbed level $\mathcal{E}_{1u}$ to lower energy without perturbing the even state $|g_1\rangle$. The process repeats for higher-order modes of the central cavity. A video is provided as SI to show this process. Note that Figures 6(b–g) are single frames taken from the video.

In our experiments, the three-cavity resonator was surrounded by a dielectric medium with refractive index n_s (Figure 1 and 3b). Since the thickness of the outer metal layers was $h_M \approx \delta$, the optical waves were not completely confined within the resonator, but could penetrate from and leak into the surrounding medium via tunneling. Figure 1 shows that the optical transmittance of a single MTM cavity with Ag layer thickness $h_M \approx \delta$ is maximum at essentially the same wavelengths λ_q expected for a single square well. The difference with the $h_M \gg \delta$ case is that the transmittance peaks of a single cavity have finite width and intensity, rather than having the shape of a Dirac delta function. Therefore, the three-cavity resonator shows essentially the same peak wavelengths (Figures 4 and 5) as if the outer metal layers of the resonator were infinitely thick.

CONCLUSIONS

This article demonstrates that the SFA is a powerful tool to investigate the coupling of resonance modes in metal-dielectric multilayers. Mode dispersion can be measured rapidly, extensively, continuously, and accurately in a single sweep of cavity thickness using one resonator, eliminating the time and cost of fabricating many fixed-thickness resonators. The experimental dispersion curve of a symmetric three-cavity resonator showed a pattern of wavelength splitting as a function of the central cavity thickness that is qualitatively different from those of a single cavity and two-cavity resonator. To understand these findings, we established a framework of interpretation based on an isomorphism between the optical field in metal-dielectric multilayers and a quantum particle in a one-dimensional assembly of multiple square wells. The experimental findings could be explained by adopting the

https://doi.org/10.1021/acsphotonics.1c01055
ACS Photonics XXXX, XXX, XXX–XXX

concepts, formalism, and methods of quantum theory, notably symmetry operators and the Rayleigh−Ritz variational method.

We anticipate that the SFA can be used to capture at a glance the optical response of a wide variety of resonators beyond the specific case considered in this article. For instance, a symmetric two-cavity resonator (MDMDM) can be created using a deformable dielectric material D for both cavities, e.g., a soft transparent elastomer such as poly(dimethyl-siloxane) (PDMS). The thickness of the cavities will decrease symmetrically in response to a mechanical load applied to the outer metal layers. Moreover, the SFA can be used to investigate the coupling of cavity modes with optical excitons, which is difficult to achieve using fixed-thickness resonators.

Our findings also have implications in the design and interpretation of SFA experiments on the electrochemistry of surfaces and the application of electric fields to nanoscale fluid films. In the standard SFA setup, the fluid (D) is confined between two molecularly smooth sheets of transparent mica (T), coated on the outside with partially reflecting Ag layers (M).[40,41] The fluid thickness can be determined as a function of the resonance wavelength using an analytic expression valid for a single cavity (MT_1DT_2M) with a composite dielectric layer (T_1DT_2).[22] To apply an electric field, metal electrodes such as gold layers can be introduced at the fluid-mica interfaces.[36−38] However, these layers act as additional mirrors and create a multicavity resonator, producing additional features that should be analyzed using more advanced theoretical tools such as quantum theory.

MATERIALS AND METHODS

MTM Fabrication and Preliminary Characterization. The MTM cavities were created by depositing layers of Ag and transparent indium−tin-oxide (ITO), respectively with target thickness 30 and 80 nm, on cylindrical glass lenses with radius R = 2 cm. The lenses had 1 cm diameter, 4 mm thickness, 60/40 scratch/dig surface quality, centration wedge angle <5 arcmin, and irregularity (interferometer fringes) $\lambda/2$ at a wavelength of 630 nm. Ag was chosen for its large extinction coefficient $\kappa > 1 \gg n$, ensuring a high reflectivity and an approximately real negative permittivity in the metal layers.[14] ITO was chosen for its transparency ($n > 1 \gg \kappa$) and straightforward deposition via DC sputtering. For both Ag and ITO layers, the growth rate was 0.16 nm/s, the presputtering pressure was 3×10^{-5} mbar, and the sputtering pressure was 4.6×10^{-2} mbar. The power was 20 W for Ag and 40 W for ITO. The thickness and refractive index of Ag and ITO were determined in planar glass slides by ellipsometry, including extinction coefficients.

SFA Measurements. The SFA Mark III by Surforce LLC, USA was used in the experiments.[40] The elastic constant of the cantilever supporting the bottom surface was 900 N/m (Figure 2b). The central cavity between the surface-supported MTM cavities was initially filled with nitrogen, but mechanical vibrations blurred the transmitted spectra (not shown). A 40 μL droplet of silicone oil (PDMS from VWR/Prolabo #84543.290, nominal viscosity 20 cSt and refractive index n = 1.40 @ 589 nm) was infiltrated in the cavity to reduce the vibrations.

Transmission spectra were obtained by illuminating the three-cavity resonator under normal incidence with white light from a halogen lamp. The transmitted light was collected through the entrance slit of an imaging spectrograph (PI Acton Spectra Pro 2300i) aligned with the x-axis of the top cylinder (Figure 3b) and recorded with a high-sensitivity CCD camera (Andor Newton DU940P−FI). Only a small region of the surface surrounding the contact position was considered, such that $r \leq 0.15$ mm $\ll R$, equivalent to a sphere-plane geometry (Figure 1).[23] A CCD camera image showed the transmitted intensity I as a function of the wavelength λ and position r (Figure 5). Multibeam interference created resonance peaks in an image, i.e., local maxima of the 2d intensity function $I(\lambda, r)$, corresponding to constructive interference. CCD images were recorded at constant time intervals Δt = 0.7 s while decreasing or increasing d. Intensity spectra $I(\lambda, r = 0)$ at the contact position were extracted from each image and stacked in sequence to create $I(\lambda, t)$ spectrograms, where t is the elapsed time (Figure 4a).

Scattering Matrix Method. Transmitted spectra were simulated using a 2 × 2 transfer matrix multiplication method for stratified optical media (also known as scattering matrix method),[15,54] with refractive indices determined by ellipsometry for Ag and ITO, and nominal value for silicone oil. Details on the method implementation are given in the Supporting Information.

ASSOCIATED CONTENT

Supporting Information

The Supporting Information is available free of charge at https://pubs.acs.org/doi/10.1021/acsphotonics.1c01055.

Details on the transfer matrix multiplication method; Discussion on the Helmholtz−Schrödinger isomorphism under oblique incidence; Calculations of the resonance splitting and hybridization coefficients for the two-cavity and three-cavity resonators (PDF)

Video showing the electric field within a three-cavity resonator as a function of position and wavelength for different thicknesses of the central cavity (AVI)

AUTHOR INFORMATION

Corresponding Authors

Bruno Zappone − *Consiglio Nazionale delle Ricerche − Istituto di Nanotecnologia (CNR-Nanotec), 87036 Rende, CS, Italy;* orcid.org/0000-0003-3002-4022; Email: bruno.zappone@cnr.it

Vincenzo Caligiuri − *Consiglio Nazionale delle Ricerche − Istituto di Nanotecnologia (CNR-Nanotec), 87036 Rende, CS, Italy; Università della Calabria − Dipartimento di Fisica, 87036 Rende, CS, Italy;* orcid.org/0000-0003-1035-4702; Email: vincenzo.caligiuri@unical.it

Authors

Aniket Patra − *Università della Calabria − Dipartimento di Fisica, 87036 Rende, CS, Italy; Istituto Italiano di Tecnologia (IIT) − Optoelectronics Research Line, 16163 Genova, Italy*

Roman Krahne − *Istituto Italiano di Tecnologia (IIT) − Optoelectronics Research Line, 16163 Genova, Italy;* orcid.org/0000-0003-0066-7019

Antonio De Luca − *Consiglio Nazionale delle Ricerche − Istituto di Nanotecnologia (CNR-Nanotec), 87036 Rende, CS, Italy; Università della Calabria − Dipartimento di Fisica, 87036 Rende, CS, Italy;* orcid.org/0000-0003-2428-9075

Complete contact information is available at: https://pubs.acs.org/10.1021/acsphotonics.1c01055

https://doi.org/10.1021/acsphotonics.1c01055
ACS Photonics XXXX, XXX, XXX−XXX

Notes

The authors declare no competing financial interest.

■ ACKNOWLEDGMENTS

We thank Dr. Giulia Biffi for providing useful insights into the hybridization of atomic orbitals in molecular theory. We also thank Prof. Francesco Plastina for fruitful discussions and manuscript revision. We acknowledge funding from the European Union's Horizon 2020 Research and Innovation Programme under Grant Agreement No. 777222 (Project ATTRACT − TEHRIS).

■ REFERENCES

(1) Dragoman, D.; Dragoman, M. *Quantum-Classical Analogies*; Springer-Verlag: Berlin, Germany, 2004.
(2) Longhi, S. Quantum-optical analogies using photonic structures. *Laser Photonics Rev.* **2009**, *3* (3), 243−261.
(3) Alaeian, H.; Dionne, J. A. Parity-time-symmetric plasmonic metamaterials. *Phys. Rev. A: At., Mol., Opt. Phys.* **2014**, *89* (3), 033829.
(4) Alaeian, H.; Dionne, J. A. Non-hermitian nanophotonic and plasmonic waveguides. *Phys. Rev. B: Condens. Matter Mater. Phys.* **2014**, *89* (7), 1−9.
(5) Rechcińska, K.; Król, M.; Mazur, R.; Morawiak, P.; Mirek, R.; Łempicka, K.; Bardyszewski, W.; Matuszewski, M.; Kula, P.; Piecek, W.; Lagoudakis, P. G.; Piętka, B.; Szczytko, J. Engineering spin-orbit synthetic Hamiltonians in liquid-crystal optical cavities. *Science* **2019**, *366* (6466), 727−730.
(6) Hsu, C. W.; Zhen, B.; Stone, A. D.; Joannopoulos, J. D.; Soljačić, M. Bound states in the continuum. *Nat. Rev. Mater.* **2016**, *1* (9), 16048.
(7) Azzam, S. I.; Kildishev, A. V. Photonic bound states in the continuum: From basics to applications. *Adv. Opt. Mater.* **2021**, *9* (1), 2001469.
(8) Marinica, D. C.; Borisov, A. G.; Shabanov, S. V. Bound states in the continuum in photonics. *Phys. Rev. Lett.* **2008**, *100* (18), 183902.
(9) Lee, J.; Zhen, B.; Chua, S. L.; Qiu, W. J.; Joannopoulos, J. D.; Soljacic, M.; Shapira, O. Observation and differentiation of unique high-Q optical resonances near zero wave vector in macroscopic photonic crystal slabs. *Phys. Rev. Lett.* **2012**, *109* (6), 067401.
(10) Liu, V.; Povinelli, M.; Fan, S. H. Resonance-enhanced optical forces between coupled photonic crystal slabs. *Opt. Express* **2009**, *17* (24), 21897−21909.
(11) Suh, W.; Solgaard, O.; Fan, S. Displacement sensing using evanescent tunneling between guided resonances in photonic crystal slabs. *J. Appl. Phys.* **2005**, *98* (3), 033102.
(12) Sadreev, A. F.; Maksimov, D. N.; Pilipchuk, A. S. Gate controlled resonant widths in double-bend waveguides: bound states in the continuum. *J. Phys.: Condens. Matter* **2015**, *27* (29), 295303.
(13) Gaponenko, S. *Introduction to Nanophotonics*; Cambridge University Press: Cambridge, UK, 2010.
(14) Caligiuri, V.; Palei, M.; Biffi, G.; Artyukhin, S.; Krahne, R. A semi-classical view on epsilon-near-zero resonant tunneling modes in metal/insulator/metal nanocavities. *Nano Lett.* **2019**, *19* (5), 3151−3160.
(15) Fowles, G. R. *Introduction to Modern Optics*; Dover: New York, NY, 1989.
(16) Kasap, S. O. *Optoelectronics & Photonics: Principles & Practices*, 2nd ed.; Prentice Hall, 2001.
(17) Caligiuri, V.; Dhama, R.; Sreekanth, K. V.; Strangi, G.; De Luca, A. Dielectric singularity in hyperbolic metamaterials: The inversion point of coexisting anisotropies. *Sci. Rep.* **2016**, *6* (1), 20002.
(18) Born, M.; Wolf, E. *Principles of Optics*; Pergamon Press: Oxford, UK, 1980.
(19) Siegman, A. E. *Lasers*; University Science Books, 1986.
(20) Gagliardi, G.; Loock, H. P. *Cavity-Enhanced Spectroscopy and Sensing*; Springer: Berlin, 2014.
(21) Li, Z.; Butun, S.; Aydin, K. Large-area, lithography-free super absorbers and color filters at visible frequencies using ultrathin metallic films. *ACS Photonics* **2015**, *2*, 183−188.
(22) Israelachvili, J. N. Thin film studies using multiple-beam interferometry. *J. Colloid Interface Sci.* **1973**, *44*, 259−272.
(23) Israelachvili, J. N. *Intermolecular and Surface Forces*; Academic Press: Waltham, MA, 2011.
(24) Nahvi, E.; Liberal, I.; Engheta, N. Nonperturbative effective magnetic nonlinearity in ENZ media doped with Kerr dielectric inclusions. *ACS Photonics* **2019**, *6* (11), 2823−2831.
(25) Yao, J.; Liu, Z. W.; Liu, Y. M.; Wang, Y.; Sun, C.; Bartal, G.; Stacy, A. M.; Zhang, X. Optical negative refraction in bulk metamaterials of nanowires. *Science* **2008**, *321* (5891), 930−930.
(26) Bruno, V.; DeVault, C.; Vezzoli, S.; Kudyshev, Z.; Huq, T.; Mignuzzi, S.; Jacassi, A.; Saha, S.; Shah, Y. D.; Maier, S. A.; Cumming, D. R. S.; Boltasseva, A.; Ferrera, M.; Clerici, M.; Faccio, D.; Sapienza, R.; Shalaev, V. M. Negative refraction in time-varying strongly coupled plasmonic-antenna-epsilon-near-zero systems. *Phys. Rev. Lett.* **2020**, *124* (4), 043902.
(27) Kuttruff, J.; Garoli, D.; Allerbeck, J.; Krahne, R.; De Luca, A.; Brida, D.; Caligiuri, V.; Maccaferri, N. Ultrafast all-optical switching enabled by epsilon-near-zero-tailored absorption in metal-insulator nanocavities. *Comm. Phys.* **2020**, *3* (1), 114.
(28) Khurgin, J. B.; Clerici, M.; Bruno, V.; Caspani, L.; DeVault, C.; Kim, J.; Shaltout, A.; Boltasseva, A.; Shalaev, V. M.; Ferrera, M.; Faccio, D.; Kinsey, N. Adiabatic frequency shifting in epsilon-near-zero materials: The role of group velocity. *Optica* **2020**, *7* (3), 226−231.
(29) Biswas, S.; Whitney, W. S.; Grajower, M. Y.; Watanabe, K.; Taniguchi, T.; Bechtel, H. A.; Rossman, G. R.; Atwater, H. A. Tunable intraband optical conductivity and polarization-dependent epsilon-near-zero behavior in black phosphorus. *Sci. Adv.* **2021**, *7* (2), 2100087.
(30) Ghasemzadeh, F.; Rashed, A. R.; Caglayan, H. Phase singularity annihilation in plasmonic nano-apertures via epsilon-near-zero metamaterials. *Appl. Photonics* **2021**, *6* (1), 016101.
(31) Nefedov, I. S.; Rubi, J. M. Casimir forces exerted by epsilon-near-zero hyperbolic materials. *Sci. Rep.* **2020**, *10* (1), 16831.
(32) Edwards, B.; Alu, A.; Young, M. E.; Silveirinha, M.; Engheta, N. Experimental verification of epsilon-near-zero metamaterial coupling and energy squeezing using a microwave waveguide. *Phys. Rev. Lett.* **2008**, *100* (3), 033903.
(33) Poddubny, A.; Iorsh, I.; Belov, P.; Kivshar, Y. Hyperbolic metamaterials. *Nat. Photonics* **2013**, *7* (12), 948−957.
(34) Caligiuri, V.; Palei, M.; Biffi, G.; Krahne, R. Hybridization of epsilon-near-zero modes via resonant tunneling in layered metal-insulator double nanocavities. *Nanophotonics* **2019**, *8* (9), 1505.
(35) Caligiuri, V.; Biffi, G.; Patra, A.; Pothuraju, R.; De Luca, A.; Krahne, R. One-dimensional epsilon-near-zero crystals. *Adv. Photonics Res.* **2021**, *2*, 2100053.
(36) van Engers, C. D.; Balabajew, M.; Southam, A.; Perkin, S. A 3-mirror surface force balance for the investigation of fluids confined to nanoscale films between two ultra-smooth polarizable electrodes. *Rev. Sci. Instrum.* **2018**, *89* (12), 123901.
(37) Wieser, V.; Bilotto, P.; Ramach, U.; Yuan, H.; Schwenzfeier, K.; Cheng, H.-W.; Valtiner, M. Novel in situ sensing surface forces apparatus for measuring gold versus gold, hydrophobic, and biophysical interactions. *J. Vac. Sci. Technol., A* **2021**, *39* (2), 023201.
(38) Zeng, H.; Tian, Y.; Anderson, T. H.; Tirrell, M.; Israelachvili, J. N. New SFA techniques for studying surface forces and thin film patterns induced by electric fields. *Langmuir* **2008**, *24* (4), 1173−1182.
(39) Tivony, R.; Klein, J. Modifying surface forces through control of surface potentials. *Faraday Discuss.* **2017**, *199* (0), 261−277.
(40) Israelachvili, J. N.; McGuiggan, P. M. Adhesion and short-range forces between surfaces. Part I: New apparatus for surface force measurements. *J. Mater. Res.* **1990**, *5*, 2223−2231.
(41) Israelachvili, J.; Min, Y.; Akbulut, M.; Alig, A.; Carver, G.; Greene, W.; Kristiansen, K.; Meyer, E.; Pesika, N.; Rosenberg, K.;

https://doi.org/10.1021/acsphotonics.1c01055
ACS Photonics XXXX, XXX, XXX−XXX

Zeng, H. Recent advances in the surface forces apparatus (SFA) technique. *Rep. Prog. Phys.* **2010**, *73* (3), 036601.
(42) Messiah, A. *Mécanique Quantique*; Dunod: Paris, 1964.
(43) Griffiths, J. G. *Introduction to Quantum Mechanics*; Prentice Hall: New Jersey, USA, 1995.
(44) Eisberg, R. M.; Resnick, R. *Quantum Physics of Atoms, Molecules, Solids, Nuclei, and Particles*; John Wiley & Sons, 1985.
(45) Gasiorowicz, S. *Quantum Physics*, 3rd ed.; John Wiley & Sons: Hoboken, NJ, 1998.
(46) Liu, B.; Fu, L.-B.; Yang, S.-P.; Liu, J. Josephson oscillation and transition to self-trapping for Bose−Einstein condensates in a triple-well trap. *Phys. Rev. A: At., Mol., Opt. Phys.* **2007**, *75* (3), 033601.
(47) Haus, H.; Huang, W. Coupled-mode theory. *Proc. IEEE* **1991**, *79* (10), 1505−1518.
(48) Fan, S. H.; Suh, W.; Joannopoulos, J. D. Temporal coupled-mode theory for the Fano resonance in optical resonators. *J. Opt. Soc. Am. A* **2003**, *20* (3), 569−572.
(49) Li, H.; Alù, A. Temporal switching to extend the bandwidth of thin absorbers. *Optica* **2021**, *8* (1), 24−29.
(50) Zhang, H.; Abhiraman, B.; Zhang, Q.; Miao, J.; Jo, K.; Roccasecca, S.; Knight, M. W.; Davoyan, A. R.; Jariwala, D. Hybrid exciton-plasmon-polaritons in van der Waals semiconductor gratings. *Nat. Commun.* **2020**, *11* (1), 3552.
(51) Bransden, B. H.; Joachain, C. J. *Physics of Atoms and Molecules*; Longman Publishing Group: UK, 1982.
(52) Marte, M. A. M.; Stenholm, S. Paraxial light and atom optics: The optical Schrodinger equation and beyond. *Phys. Rev. A: At., Mol., Opt. Phys.* **1997**, *56* (4), 2940−2953.
(53) Atkins, P.; Friedman, R. *Molecular Quantum Mechanics*; Oxford: Oxford, UK, 2005.
(54) Zappone, B.; Zheng, W. C.; Perkin, S. Multiple-beam optical interferometry of anisotropic soft materials nanoconfined with the surface force apparatus. *Rev. Sci. Instrum.* **2018**, *89* (8), 085112.

https://doi.org/10.1021/acsphotonics.1c01055
ACS Photonics XXXX, XXX, XXX−XXX